Vertical wind profiling from the troposphere to the lower mesosphere based on high resolution heterodyne near-infrared spectroradiometry

Alexander V. Rodin[1,2] , Dmitry V. Churbanov[1], Sergei G. Zenevich[1], Artem Yu. Klimchuk[1,3], Vladimir M. Semenov[3], Maxim V. Spiridonov[1,4], Iskander Sh. Gazizov[1].

[1] Moscow Institute of Physics and Technology, Dolgoprudny, Russia
[2] Space Research Institute, Moscow, Russia
[3] Samsung R&D Institute, Moscow, Russia
[4] Prokhorov General Physics Institute, Moscow, Russia

Correspondence to: Alexander V. Rodin (alexander.rodin@phystech.edu)

Abstract. We propose a new technique of remote wind measurements based on Doppler analysis of a CO_2 absorption line in the 1.605 μm overtone band measured in the direct Sun observation geometry. Heterodyne spectroradiometric measurements of the solar radiation passed through the atmosphere provide an unprecedented spectral resolution up to $\lambda/\delta\lambda \sim 6\cdot10^7$ with a signal-to-noise ratio more than 100. The shape of the individual rotational line profile provides an unambiguous relationship between the offset from the line centre and the altitude where the respective part of the line profile is formed. Therefore, an inverse problem may be posed in order to retrieve vertical distribution of wind, with retrievals the vertical resolution compromised by a spectral resolution and signal-to-noise ratio of the measurements. A close coincidence between measured and synthetic absorption line is reached, with retrieved wind profiles between the surface and 50 km being in a good agreement with reanalysis models. This method may pose an alternative to widely employed lidar and radar techniques.

1 Introduction

In spite of the tremendous progress in remote sensing during last decades, atmospheric dynamics still remains hard to assess by direct measurements. To date, the most reliable means of the remote wind field measurement are Doppler radars whose sounding range extends up to the lower thermosphere (Woodman and Guillien, 1974, Hocking, 1997, Hysell et al., 2014). Doppler lidars typically operating in the infrared spectral range are widely used at smaller scales (Eberhard and Schotland, 1980, Bruneau et al., 2015). These methods are based on active sounding of the medium by a powerful source (laser of radar beam), implying significant required resources in mass, size, and power consumption. In contrast with radar and lidar sounding, passive Doppler spectroradiometry has received much less attention in atmospheric studies. Recent developments in the microwave Doppler wind velocimetry have been reported by Newnham et al. (2016). The authors argue that in the stratosphere and lower mesosphere, passive high resolution spectroradiometry in the microwave remain one of the most effective technique of direct wind monitoring. Not only provides heterodyne spectroscopy information about wind field in the Earth atmosphere, but also in the atmospheres of other planets. Taking advantage of passive observations capabilities of sounding remote objects

at arbitrary distances, high resolution heterodyne spectroscopy in the microwave and mid-infrared spectral ranges has provided an opportunity to measure winds in the atmospheres of Venus, Mars, and Titan by means of ground-based telescopes (Kostiuk et al., 1983, Sornig et al., 2012). High resolution spectroscopic studies with traditional echellé or Fabri-Perot spectrometers in the visible spectral range have been also employed for wind measurements in the atmospheres of Earth and other planets from the ground-based telescope (Widemann et al., 2007) and Earth-orbiting satellite (Killen at al., 2006). However, direct wind measurements beyond the troposphere of the Earth, as well as of other Solar System planets, remain largely peculiar studies rather than well-established technique.

As radiometric Doppler velocimetry requires an extraordinary spectral resolution $\lambda/\delta\lambda \sim 10^8$, which could be most effectively implemented using heterodyne detection technique. However, instruments for atmospheric heterodyne radiometry operating in the microwave and terahertz ranges are typically heavyweight and expensive, and hence their implementations at spaceborne and airborne platforms are limited. Ground-based stations equipped with such instruments are in the limited use because of relatively high cost as well. We propose a technique that allows Doppler measurements in the near-infrared spectral range by means of a compact, lightweight, and simple near-infrared spectroradiometer in the direct Sun observation mode. The heterodyne method is rarely used for spectroscopic measurements in this range for various reasons. First of all, there is a fundamental limit to the signal level when observing an extended object, as the field of view of any heterodyne radiometer is constrained by a diffraction limit due to antenna theorem (Siegman, 1966). Thus if the Sun is used as a light source for atmospheric sounding, an entrance aperture as small as 0.3 mm in diameter would provide the maximal signal to be put into the heterodyne instrument working at 1.605 µm. On the other hand, the shorter wavelength, the higher photon energy, and quantum limit of the heterodyne detection sensitivity increases accordingly. For instance, for the wavelength $\lambda = 1.605$ µm, the quantum limit in terms of noise-equivalent power (NEP) is $\sim 10^{-19}$ W/Hz. With the resolved bandwidth $B = 3$ MHz and reasonable exposure time τ up to few minutes, the quantum limit constrains heterodyne detection by a minimal level of spectral brightness of $p = \frac{hc}{\lambda\sqrt{B\tau}} \approx 10^{-24}$ W/Hz. Therefore, applications of heterodyne detection in the shortwave infrared range is limited to the cases where either Sun or artificial non-thermal light sources characterized by high spectral brightness are used, such as LEDs or lasers.

Several examples of near-infrared heterodyne spectroradiometers utilizing Sun as a radiation source have been recently developed for the purpose of greenhouse gas measurements, including methane and carbon dioxide (Rodin et al., 2014, Wilson et al, 2014, Melroy, 2015, Kurz et al., 2016, Hoffman et al., 2016, Zenevich et al., 2019, Deng et al., 2019, Wang et al., 2019). Weidmann et al., (2017) took advantage of the compact design of a fiber-based heterodyne spectroradiometer and proposed a cubesat-class mission for methane isotopologue measurements. The above mentioned authors focused on the advantage of high resolution spectroscopy in sensitive measurements of absorber amounts and distinguishing isotopes of the same species. In this work we analyze capabilities of this method to fetch spectroscopic information for remote Doppler velocimetry.

2 The instrumental setup

2.1 Fundamentals of tuneable diode laser heterodyne spectroradiometry

The basic principles of the diode laser heterodyne spectroradiometry (TDLHS) have been presented in detail in previous works,
65   e.g. in Rodin et al. (2014), Kurz et al. (2016), Zenevich et al. (2019). Here we briefly repeat the core information important for Doppler measurements. In contrast with conventional microwave heterodyne spectroradiometry, TDLHS operates with a tunable local oscillator (LO) – a diode laser with distributed feedback (DFB), characterized with a bandwidth of about 2MHz and capable of changing its radiation frequency in a broad spectral range. Typically, two parameters are employed to control DFB laser radiation frequency – its temperature and injection current. Temperature affects the resonant frequency through the
70   period of an embedded Bragg grating, while pumping current impacts both grating period (through temperature variations according to absorbed power) and refractive index (through charge carrier density). Commercial DFB lasers are supplied with embedded Peltier coolers and thermal sensors, so both parameters could be precisely controlled by external electronics.

We apply the algorithm of LO sweeping with locking to reference absorption line, as described in Rodin et al. (2014). According to this algorithm, temperature controller is set at constant value, while pumping current is modulated by a piecewise
75   linear saw-edged function. Both laser power and wavelength change accordingly. Signal acquired simultaneously in the heterodyne channel is characterized by linear growth of the received power according to changing LO intensity, and by a random heterodyne component:

$$i_{het} = D\left(E_S E_{LO} + E_S^* E_{LO}^*\right)$$
$$= D\mathrm{Re} \int_0^\infty g_{LO}(\omega')d\omega' \int_0^\infty F_S(\omega)\exp\left[-i(\omega-\omega')t + i\varphi_S(t) - i\varphi_{LO}(t)\right]d\omega, \tag{1}$$

where D is the detector responsivity, g_{LO} and F_S are power spectral densities of the LO and solar light at LO frequency, while
80   φ_{LO} and φ_S are their respective phases. The power spectrum of the beat signal is proportional to the convolution of power spectra related to the signal F_S and local oscillator S_{LO}, respectively:

$$S_{het}(\omega) = 2D \int_0^\infty S_{LO}(\nu-\omega)d\omega' \int_0^\infty F_S(\nu)\,d\nu. \tag{2}$$

As the analyzed solar radiation is not expected to reveal features narrower than the LO bandwidth, i.e. F_S may be assumed constant within the bandwidth B, corresponding to the peak of S_{LO}, which in turn may be replaced by delta function, the
85   convolution in the right hand side of Eq. (2) could be reduced to a simple product. Due to the random phase factor, within a narrow frequency range with respect to LO bandpass, $\Delta\omega \le \Delta\omega_{LO}$, the heterodyne signal reveals properties of a white noise with the dispersion, proportional to the target spectral density F_S:

$$\left\langle i_{het}^2 \right\rangle = 2D B i_{LO} \cdot F_S\left(\omega_{LO}\right) \tag{3}$$

3

Therefore, to achieve heterodyning of the thermal non-coherent IR radiation, one needs, at first, to subtract a linear component from the signal associated with sweeping the LO power, and then to obtain the dispersion by square detection. Finally, appropriate exposure and data collection provides target spectrum $F_S(\omega)$ with required signal-to-noise ratio. Taking into account that the LO linewidth has an order of 2MHz, the spectral resolution of heterodyne detection is sufficient to measure Doppler shift of the absorption line in the atmosphere due to air mass motion with along line-of-sight velocities greater than 3 m/s, provided high LO stability and sufficient accuracy of intermediate frequency (IF) signal analysis. Note that sweeping the LO frequency over spectral range of interest and replacement IF spectral analysis by mere dispersion evaluation implies much simpler instrument design compared to conventional heterodyne spectroradiometers, as complex backend equipment is no longer necessary. Further details of data treatment depend on the optical scheme and should be discussed in the link with description of the experimental setup.

2.2 Experimental setup and observations

Detailed description of the experimental setup is presented in Zenevich et al. (2019). Here we shortly repeat the main information important for understanding. A sketch of the experimental laser heterodyne spectroradiometer (LHS) is presented in Figure 1. Solar radiation passed through the atmosphere is focused to the edge of a single mode silica optical fiber with core diameter ~ 10 µm by a lens with focal length f = 50 mm. A chopper installed in front of the fiber allows to record heterodyne signal with the Sun on and off. Thus the dark signal, dominated with the shot noise, and superposition of the heterodyne and dark signals are measured separately. This technique provides accurate subtraction of the shot noise unaffected by possible system drifts of the instrument. Sunlight entering the fiber has been combined with a LO radiation in a single mode silica coupler with a 5:95 coupling ratio. According to the antenna theorem (Siegman, 1968), single mode fiber geometric aperture factor ~$2.6 \cdot 10^{-8}$ cm^2, which corresponds to field of view ~ 0.006º. This is close to the maximum available for heterodyne detection and therefore does not limit the instrument sensitivity (Rodin et al., 2014). An automated SkyWatcher EQ6 PRO SynScan equatorial mount equipped with QHY5-II guide camera was used to track the Sun during observations.

Radiation of the NEL DFB laser serving as a LO is split in 50:50 proportion, with one portion being coupled with solar radiation in the heterodyne channel, and another portion being put into the reference cell. All fiber-optical connections in both the heterodyne and the reference channels are made by welding with the exception of two FC/APC angled connectors to LO and to the telescope, to avoid undesired reflection, which may otherwise significantly contaminate the signal with parasite interference pattern. Frequency ramping in the range 6230.2±0.35 cm^{-1} was provided due to modulation of the pumping current by a chain of pulses, with a pulse length of 39.4 ms, a dead time of 10.6 ms, and a stepwise current growth within a pulse with a step length of 200 µs. The cell filled with CO_2 at a pressure of 13 Torr is an off-axis resonator with the input and output mirrors reflectivity R_{in} = 0.9998 and R_{out} = 0.98, respectively, which provides the effective optical path length ~30 m. This path allows for reliable measurement of Doppler-broadened contour of the weak absorption line in the 1.605 µm band by means of the integrated cavity output spectroscopy (ICOS) technique (Moyer et al., 2008). Negative feedback between the

4

detected line position in the reference cell and diode laser crystal temperature has been organized in order to stabilize LO frequency ramping and to avoid drifts, with the crystal temperature correction accuracy of 10^{-4} K. Although line shape in the ICOS cell is different from the Voigt profile, it does not affect LO stabilization procedure, as the only information used in the feedback concerns with the peak position. After coupling solar radiation with the LO, single mode fiber transmits the signal into Hamamatsu InGaAs p-i-n diode photodetector serving as a heterodyne mixer. Then the beat signal is analyzed with backend electronics.

After the transimpedance preamplifier, the signal is passed through a consecutive low-pass filter, another amplifier and high-pass filter, that limits its bandwidth to 0.2…3 MHz. The preamplifier circuit is connected to a Rohde & Schwarz RTO 1012 digital oscilloscope at two points: after the IF receiver and just after transimpedance preamplifier. The latter signal repeats the LO pumping current pulse shape and is utilized for oscilloscope synchronization with the LO ramping cycle. The first is used for dispersion evaluation and data collection. The oscilloscope translates the signal into digital sequence with the rate of 20 000 points per second, then calculates the dispersion and averages data in a similar way as it has been previously done by Wilson et al. (2014) and Kurz et al. (2016). The oscilloscope communicates with the PC by Ethernet channel, while the other parts of the setup, including LO control system and Sun tracker, are connected by USB. Instrument control and data transfer are implemented based on LabView platform.

As the correct frequency calibration over the whole range of LO ramping is crucial for Doppler analysis of the atmospheric absorption, we employed another reference channel based on a Fabri-Perot etalon. Frequency calibrations were done offline, as described in Rodin et al. (2014), and utilized for processing and interpretation of atmospheric absorption measurements. In order to estimate the accuracy of frequency absolute stabilization by the reference cell and relative calibration by Fabri-Perot etalon, deviations in LO frequency ramping from the prescribed sequence have been tracked along several hours. These tests have shown a root mean squares deviation of 1.5 MHz in the vicinity of the reference CO_2 line, and 6 MHz in the rest of the LO ramping range.

Several observation sessions have been carried out during the summer 2018 under clear sky conditions. The instrument has been installed at the top of one of the buildings at MIPT campus at the North of Moscow city, with coordinates 55.929036º N, 37.521506º E, about 50 m above the sea level. Data were collected for ~10 min, to reach signal-to-noise level of 100. The details of observations and some key characteristics of the retrieved spectra are presented in Table 1.

3 Wind profile retrievals

3.1 Raw data treatment

Once the heterodyne signal is obtained, one needs to subtract corresponding dark signal with the solar channel being closed by a chopper. The next step is to eliminate the baseline slope caused by the modulation of LO power. Since the heterodyne signal and shot noise have the same statistical nature, being proportional to the power absorbed by a photomixer, this slope cannot be eliminated by dark signal subtraction and requires model approximation of the spectral continuum outside the

observed absorption line. After subtraction of dark signal, heterodyne signal should be normalized by assumed spectral continuum (baseline) approximated by square polynomial to obtain the final transmission spectrum of the atmosphere.

155   Consecutive steps of raw data treatment are presented in Figure 2 (a – c). In Figure 2a one could notice a baseline distortion in the reference channel caused by the residual interference in the ICOS multipass cell. This distortion may be eliminated by a precise adjustment of the entrance beam. However, this channel is only used for determination of the line peak position, which is not sensitive to the baseline variations.

Further treatment of LHS data implies comparison with a synthetic spectrum of the atmospheric transmission. Since in the
160   narrow field of view of the LHS the scattered component is negligible compared to direct solar radiation, the simulation of atmospheric spectra is straightforward. In addition to the target CO_2 line R2 $14^01 \leftarrow 00^00$ at 6230,22 cm-1, other CO_2 lines at 6230,25 cm^{-1}, 6230,02 cm^{-1} and 6229,98 cm^{-1} have also been included in the calculations. Other atmospheric species, including water vapor, do not affect this spectral range with features that could be distinguished from the spectral continuum. Based on HITRAN-2016 data (Gordon et al., 2017), a model of the atmospheric transmission spectrum has been constructed. In the
165   calculations we used Voight profile and neglected line mixing and other fine effects that may affect line shape in its far wings (Armstrong, 1982, Bulanin et al., 1984, Boone et al., 2011). Although such a simplistic approach may appear insufficient for analysis of a fully resolved line profile, experiments presented below show that the model fits observations within data errors. Peculiar exceptions, including poor fitting to the Doppler-broadened line core described below, do not affect wind retrievals as the contribution of this narrow spectral range to the retrieval procedure is negligible.

170   The modelled atmosphere includes 100 uniform layers with constant gas composition, pressure, temperature, and wind. The upper boundary of the modelled atmosphere is determined by the condition that maximal absorption in the uppermost layer did not exceed 0.1% of the total absorption. The model only included gas absorption in the lines mentioned above, whereas scattering processes have been neglected. Minor effects of second order in terms of line-of-sight curvative, such as atmospheric refraction and sphericity of the atmosphere have been neglected as well. The model does not pretend to provide precise
175   calculation of the net absorption, as if were required for CO_2 column amounts retrievals, whereas it is line shape rather than line depth, that contains information about line-of-sight wind component. An example of line shape fit by radiative transfer model involving Doppler line distortion is presented in Figure 2 (c) by red curve. It is evident that the line shape in the atmospheric column shown in Figure 2 (c) is different from that detected in the reference cell (Figure 2, a). The atmospheric line reveals a sharper tip and broader wings due to superposition of absorption characterized by different broadening at different
180   altitudes. Broader wings dominated by collisional Lorentz broadening profile are formed in the troposphere, whereas a narrow, Doppler-broadened tip is formed in the stratosphere and mesosphere. It is this line shape, that provides information about vertical variations of atmospheric conditions, that provides a clue to wind profile retrievals from LHS data.

Wind affects the model spectrum by Doppler shift of the line at each particular model layer, with transmittance spectrum line shape and absorption value corresponding to the local pressure, temperature and CO_2 concentration. Indeed, lower atmospheric
185   layers contribute more effectively to the wings of line profile, whereas line peak dominated with Doppler thermal broadening is formed at higher altitudes. Therefore, providing non-uniform profile of wind projection on the line of sight, the observed

line profile is distorted rather than shifted in frequency scale. This fact gives an opportunity of line-of-sight component of the wind profile retrieval based on analysis of the resolved line shape.

3.2 Solution to the inverse problem of wind profiling based on high resolution NIR absorption spectrum

190   Inverse problems of radiative transfer similar to those stated above, i.e. wind projection profile retrievals from absorption line shape observed through the atmospheric column suffers from ill-posedness. This term means that a solution is not unique and/or reveals instability versus small variations of data such a solution is based on (Hadamard, 1902). Since TDLHS introduces a certain noise level to data by nature, noisy data forces the instability of a solution unless special measures for solution regularization is taken. In this work we consider the generalized residual method of regularization (GRM), similar in
195   many aspects to Tikhonov regularization, yet highly efficient in cases when some *a priori* assumption on solution properties could be made (Tikhonov, 1998).

Let us consider a radiative transfer model taking into account Doppler distortion of the absorption spectrum:

$$\int_0^H \sigma\left(v - \frac{v_0 \sin(\theta)}{c} U(z), z\right) \rho(z) dz \ = \ \tau(v), \tag{4}$$

where $\tau(v) = -\ln T(v) \cdot \cos\theta$ is optical depth normalized for vertical path at wavenumber v, $T(v)$ is observed atmospheric
200   transmission, θ is the Sun zenith angle, $\rho(z)$ is assumed number density of CO_2 molecules, $U(z)$ is assumed vertical profile of wind projection on the line of sight, c is the speed of light, v_0 is a wavenumber of the line centre and the function $\sigma(v, z)$ is a model absorption crossection at wavenumber v and altitude z per molecule calculated according to the algorithm described above. Equation (4) may be rewritten in the operator form:

$$\hat{A}\{\overline{U}, \overline{\rho}\} = \overline{\tau}; \ (\overline{U}, \overline{\rho}) \in W_2^1; \tau \in L_2, \tag{5}$$

205   or, assuming a nearly uniform vertical distribution of carbon dioxide in the atmospheric column and replacing vector $\overline{\rho}$ by a scalar parameter ρ,

$$\hat{A}\overline{U} \cdot \rho = \overline{\tau}; \ \rho \in R; \overline{U} \in W_2^1; \overline{\tau} \in L_2. \tag{6}$$

It has been first noticed by Tikhonov (1943) that a solution $\overline{U}$ to (6) reveals stability in RHS provided it is searched for on a compact set $M \subset W_2^1$. GRM implies the introduction of a stabilizing functional $\Omega(U, \rho)$ which is physically sensible and
210   obeys special properties, e.g. is concave and semi-continuous, to provide method convergence (Amato and Hughes, 1991). Such a functional may be constructed according to the maximum entropy method:

$$\Omega_\varepsilon(U) = \int_0^H g(U(z)) \ln(g(U(z)) + 1) dz \ + \ \int_0^H g(\partial U_z(z)) \ln\left(g(\partial U_z(z)) + 1|\right) dz, \tag{7}$$

7

Function $g(U)$ is introduced to provide convexity of the functional $\Omega_\varepsilon(U)$, $g(U)$ is a smooth function taken in the form

$g(U) = \sqrt{U^2 + \varepsilon}$ with a small epsilon $\varepsilon = 0.001$ and the approximation property $|\Omega_\varepsilon(U) - \Omega_\varepsilon(U)| < \varepsilon k$ (k is a

constant). So that the solution should be searched for on the compact set $M = \{\Omega(\overline{U}, \overline{\rho}) \leq \Omega_\delta\}$. As a result, the solution is

obtained by constrained minimization of the stabilizing functional provided that model deviation from the dataset does not

exceed expected measurement error:

$$\overline{U}' = \arg\min \left\{ \Omega_\varepsilon(\overline{U}) : \left\| \hat{A}\overline{U} \cdot \rho - \overline{\tau} \right\| \leq \delta \right\}, \tag{8}$$

The choice of maximal entropy as a solution regularization criterion is closely related to the nature of its uncertainty. Indeed,

the vertical wind profile from the ground to mesosphere is determined by a number of factors and therefore is not expected to

obey any special properties but smoothness caused by averaging over kernels shown in Figure 3. However, it is known *a priori*

that the retrievals are based on observed line shapes (see Figure 2b), and may not contain information exceeding its limited

amounts delivered by those data. Any extra information added during data treatment process may only decrease the quality of

retrievals. Therefore, among solutions compatible with observations, those obeying minimal information would be considered

the best. Since information is by definition equivalent to entropy up to a sign, smoothing functional (7) reflecting maximal

entropy principle selects the best solution to the inverse problem (6). Once the regularization criterion is selected, the problem

(8) could be efficiently solved sequential quadratic programming methods (Spellucci, 1998), resulting in vertical profile of

wind projection on the line of sight of Sun observation.

In order to estimate potential uncertainties introduced by the retrievals, it is instructive to linearize the problem (6) in the

proximity of some assumed solution $\overline{U}_0$:

$$\hat{A}' d\overline{U} \cdot \rho = d\overline{\tau}, \tag{9}$$

where $\hat{A}'$ is an operator of the initial radiative transfer problem (6) linearized in wind velocity projection $\overline{U}$. It is convenient

to use classical Tikhonov functional which is the nonconstrained analog of the GRM method with the Lagrange additional

parameter α:

$$M^\alpha[U] = \left\| \hat{A}\overline{U} \cdot \rho - \overline{\tau} \right\|^2 + \alpha\Omega_\varepsilon(\overline{U}), \tag{10}$$

Then the Jacobian of the regularized inverse operator may be written in a matrix form, where I is a Jacobian matrix of the

subintegral function in (7):

$$\hat{K} = \left(\hat{A}'^* \hat{A}' + \alpha I \right) \hat{A}'^*, \tag{11}$$

Where α is a regularization parameter which can be determined according to the residual principle (Tikhonov, 1998). Here is

used that the function $\rho(\alpha)$ is monotonically increasing according to the α parameter $\rho(\alpha) = \| AU - \tau \|^2 = \delta^2$, in our

case we have $\alpha = 2.43e-5$. The linearized solution will take a form $\overline{U}' = \rho^{-1} \hat{K} \left(\overline{\tau} - \overline{\tau}_0 \right) + \overline{U}_0$, or $d\overline{U} = \rho^{-1} \hat{K} d\overline{\tau}$.

The averaging kernel which characterizes the sensitivity of a regularized solution $\overline{U}'$ to exact one $\overline{U}$ is defined as (see Rodgers, 2000):

$$\hat{\kappa} = \frac{\partial \overline{U}'}{\partial \overline{U}} = \hat{K} \hat{A}'. \tag{12}$$

245 Examples of averaging kernels are presented in Figure 4 depending on altitude. Each curve corresponds to that particular altitude where the exact solution is defined, so that one may consider it as a point spread functions associated with the regularization procedure. Therefore, the characteristic width of the main peak of the averaging kernel is a measure of the effective vertical resolution of the method. It is seen from Figure 4, that the resolution is higher in the lower part of the profile and reaches few km near the ground, whereas higher in altitude, it is comparable with one scale height. Another important

250 feature of the kernel is the presence of negative secondary peaks, which may, for some particular wind profiles, generate unrealistic oscillations in retrievals. Nevertheless, the shape of averaging kernels that demonstrate sharp main peaks and regular structure, provides an opportunity of sensible recovery of wind projection profiles from the lower troposphere to mesosphere with the vertical resolution better than one scale height. Note that average kernels and, hence, vertical resolution of wind retrievals is determined by collisional linewidth and signal-to-noise ratio rather than on spectral resolution of the instrument,

255 which is excessively high for such retrievals.

3.3 Results

Analysis of data received during three observation sessions in summer 2018 is presented below. Retrievals according to the algorithm described in the previous section have been compared with the atmospheric circulation model reanalysis data available in the NCAR/NCEP database (Kalnay et al., 1996). Thermal profiles based on the NCAP reanalysis were adopted

260 for the radiative transfer calculations as well. Reanalysis data with a horizontal resolution of 1 km and 37 layers in the vertical were interpolated to the location of the instrument noticed above, while their lateral variations along the line of sight during Sun observations were neglected.

Wind projection profiles on the Sun observation line of sight are presented in Figure 5 versus reanalysis data. Measured transmission spectra with best-fit radiative transfer simulations are shown at the left panels on the same Figure as well. It is

265 evident that in the case of relatively smooth wind profiles (panels a – f) the retrievals demonstrate remarkable coincidence with reanalysis data in the troposphere and reasonable agreement at higher altitudes. Although the maximal disagreement between two profiles may reach 10 m/s, as seen, for instance, in Figure 5 (a,b), the altitudes where wind projection slews into opposite direction are reproduced in most observations, with the exception of few cases (Figure 5 g,j). Sensitivity of the proposed technique is evidently insufficient to detect wind variations less than 3 m/s, which is particularly evident in the

270 profiles corresponding to low wind speeds (Figure 5 l,n). This sensitivity limit is consistent with estimated stability of the local

oscillator at the level of 1MHz (Rodin et al., 2014) and exceeds the estimate based on spectral resolution of 10 MHz. It worth noticing that variations in the absorption spectrum associated with 1 MHz Doppler shift are two orders of magnitude smaller than the width of the Doppler-broadened line tip, and cannot be distinguished in the graph by naked eye. In some spectra, characterized by remarkable difference between measured and model data (e.g. Figure 5 g,j) the retrievals reveal substantial deviation from reanalysis as well. We hypothesize that in these cases the measurements are contaminated with instrumental errors, perhaps, caused by electromagnetic influence of electronic equipment, so that the retrieval algorithm failed to reproduce those data with any reasonable wind profile. In one particular case resented in Figure 5 (n), the model fails to reproduce the very tip of CO_2 absorption line with the residual being far beyond noise level. The reason of such a deviation is not clear, perhaps, it is concerned with relatively high zenith angle and, hence, airmass factor, so that the approximation of plane-parallel atmosphere in the model calculation is no longer applicable.

Interpretation of the obtained wind projection profiles are beyond the topic of this paper. We also do not analyze retrieved amounts of carbon dioxide in the atmosphere, both column abundance and vertical distribution, which may also be inferred from high resolution NIR spectroradiometry data. These topics will be considered elsewhere. Here we only consider a potential possibility of remote wind sounding by means of simple, portable, and easy-to-use instrument.

4 Conclusion

We demonstrated a new method of wind speed remote sensing based on high resolution heterodyne NIR spectroradiometry in the mode of direct Sun observations. A laser heterodyne spectroradiometer using DFB laser as a local oscillator and multipass ICOS reference cell, allows one to measure atmospheric absorption spectrum with spectral resolution $\lambda/\delta\lambda \sim 10^7$-$10^8$ and to retrieve vertical profiles of wind speed projection on the line of sight with the accuracy of 3-5 m/s and vertical resolution varying from 2 km near the ground to 6 km in the stratosphere. The method provides accurate evaluation of wind speed shear and altitude of its reversal. Profiles characterized with complex structure and multiple reversals are reconstructed with worse accuracy. Further development of this technique is possible by implementing of multichannel photodetector configuration. This could significantly decrease the integration time and increase signal-to-noise ratio.

References

300 Amato, U. and Hughes, W.: Maximum entropy regularization of Fredholm integral equations of the first kind, Inverse problems, 7, 793-808, 1991.

Armstrong, R. L.: Line mixing in the v2 band of CO_2, Appl. Opt., 21, 2141-2145, doi:10.1364/AO.21.002141, 1982.

Boone, C. D., Walker, K. A. and Bernath, P. F.: An efficient analytical approach for calculating line mixing in atmospheric remote sensing applications, J. Quant. Spectr. Rad. Trans., 112(6), 980-989, doi:10.1016/j.jqsrt.2010.11.013, 2011.

305 Bruneau, D., Pelon, J., Blouzon, F., Spatazza, J., Genau, P., Buchholtz, G., Amarouche, N., Abchiche, A. and Aouji, O.: 355-nm high spectral resolution airborne lidar LNG: system description and first results, Appl. Opt., 54(29), 8776–8785, doi:10.1364/AO.54.008776, 2015.

Bulanin, M.O., Dokuchaev, A.B., Tonkov, M.V., & Filippov, N.N.: Influence of line interference on the vibration-rotation band shapes, J. of Quant. Spec. and Rad. Tran., 31, 6, 521-543, doi:10.1016/0022-4073(84)90059-1, 1984.

310 Deng, H., Yang, C., Wang, W., Shan, C., Xu, Z., Chen, B., Yao, L., Mai, H., Kan, R. and He, Y. Near infrared heterodyne radiometer for continuous measurements of atmospheric CO2 column concentration. Infrared Physics & Technology, doi:10.1016/j.infrared.2019.06.002, 2019.

Eberhard, W. L. and Schotland, R. M.: Dual-frequency Doppler-lidar method of wind measurement, Appl. Opt., 19(17), 2967 – 2976, doi:10.1364/AO.19.002967, 1980.

315 Gordon I.E., Rothman, L.S., Hill, C., Kochanov, R.V., Tan, Y., Bernath, P.F., Birk, M., Boudon, V., Campargue, A., Chance, K.V., Drouin, B.J., Flaud, J.-M., Gamache, R.R., Hodges, J.T., Jacquemart, D., Perevalov, V.I., Perrin, A., Shine, K.P., Smith, M.-A.H., Tennyson, J., Toon, G.C. et al.: The HITRAN2016 molecular spectroscopic database, J. Quant. Spectr. Rad. Trans., 203, 3-69, doi:10.1016/j.jqsrt.2017.06.038, 2017.

Hadamard, J.: Sur les problèmes aux dérivées partielles et leur signification physique. In: Princeton University Bulletin. Bd.

320 13, Nr. 4, 1902, ZDB-ID 1282693-5, S. 49–52.

Hocking, W. K.: Recent advances in radar instrumentation and techniques for studies of the mesosphere, stratosphere, and troposphere, Radio Sci., 32, 6, 2241–2270, doi:10.1029/97RS02781, 1997.

Hoffmann, A., Macleod, N.A., Huebner, M. and Weidmann, D.: Thermal infrared laser heterodyne spectroradiometry for solar occultation atmospheric CO_2 measurements, Atmos. Meas. Tech., 9, 5975-5996, doi:10.5194/amt-9-5975-2016, 2016.

325 Hysell, D. L., Larsen, M. F. and Sulzer, M. P.: High time and height resolution neutral wind profile measurements across the mesosphere/lower thermosphere region using the Arecibo incoherent scatter radar, J. Geophys. Res., 119, 3, 2345 – 2358, doi:10.1002/2013JA019621, 2014.

Kalnay, E., Kanamitsu, M., Kistler, R., Collins, W., Deaven, D., Gandin, L., Iredell, M., Saha, S., White, G., Woollen, J., Zhu, Y., Chelliah, M., Ebisuzaki, W., Higgins, W., Janowiak, J., Mo, K. C., Ropelewski, C., Wang, J., Leetmaa, A., Reynolds, R.,

330 Jenne, R. and Joseph, D.: The NCEP/NCAR 40-Year Reanalysis Project, Bull. of the Amer. Meteor. Soc., 77, 3, 437-472, doi:10.1175/1520-0477(1996)077<0437:TNYRP>2.0.CO;2, 1996.

Killeen, T.L., Wu, Q., Solomon, S. C., Ortland, D. A., Skinner, W. R., Niciejewski, R. J. and Gell, D. A.: TIMED Doppler Interferometer: Overview and recent results, J. Geophys. Res., 111, A10S01, doi:10.1029/2005JA011484, 2006.

Kostiuk, T., and Mumma, M.J.: Remote sensing by IR heterodyne spectroscopy, Appl. Opt., 22, 17, 2644-2654, doi:10.1364/AO.22.002644, 1983.

Kurtz, J. and O'Byrne, S.: Multiple receivers in a high-resolution near-infrared heterodyne spectrometer, Opt. Exp., 24, 21, 23838-23848, doi:10.1364/OE.24.023838, 2016.

Melroy, H.R., Wilson, E.L., Clarke, G.B., Ott, L.E., Mao, J., Ramanathan, A.K., McLinden, M.L.: Autonomous field measurements of CO_2 in the atmospheric column with the miniaturized laser heterodyne radiometer (Mini-LHR), Appl. Phys. B, 120, 4, 609–615, doi:10.1007/s00340-015-6172-3, 2015.

Moyer, E., Sayres, D., Engel, G. et al.: Design considerations in high-sensitivity off-axis integrated cavity output spectroscopy, Appl. Phys. B, 92, 467-474, doi:10.1007/s00340-008-3137-9, 2008.

Newnham, D.A., Ford, G.P., Moffat-Griffin, T. and Pumphrey, H.C.: Simulation study for measurement of horizontal wind profiles in the polar stratosphere using ground-based observations of ozone and carbon monoxide lines in the 230-250 GHz region, Atmos. Meas. Tech., 9, 3309-3323, doi:10.5194/amt-9-3309-2016, 2016.

Rodin, A., Klimchuk, A., Nadezhdinskiy, A., Churbanov, D. and Spiridonov, M.: High resolution heterodyne spectroscopy of the atmospheric methane NIR absorption, Opt. Exp., 22, 11, 13825-13834, doi:10.1364/OE.22.013825, 2014.

Rodgers, C. D.: Inverse Methods for Atmospheric Sounding: Theory and Practice, World Scientific Press, 2, Singapore, 2000.

Siegman, A.E.: The antenna properties of optical heterodyne receivers, Appl. Opt., 5, 1588-1594, doi:10.1364/AO.5.001588, 1966.

Sornig, M., Livengood, T.A., Sonnabend, G, Stupar, D., Kroetz, P.: Direct wind measurements from November 2007 in Venus upper atmosphere using ground-based heterodyne spectroscopy of CO_2 at 10 mm wavelength, Icarus, 217, 863-874, doi:10.1016/j.icarus.2011.03.019, 2012.

Spellucci, P.: Mathematical Methods of Operations Research, 47(3), 355-400, doi:10.1007/BF01198402, 1998.

Tikhonov, A.M.: On the stability of inverse problems, Dokl. Akad. Nauk SSSR, 39, 5, 195–198, 1943.

Tikhonov, A.M.: Nonlinear Ill-Posed Problems, Springer Netherlands, 1998.

Weidmann, D., Hoffmann, A., Macleod, N., Middleton, K., Kurtz, J., Barraclough, S., Griffin, D.: The Methane Isotopologues by Solar Occultation (MISO) Nanosatellite Mission: Spectral Channel Optimization and Early Performance Analysis, Remote Sens., 9, 1073-1093, doi:10.3390/rs9101073, 2017.

Widemann, T., Lellouch, E., Campargue, A.: New wind measurements in Venus' lower mesosphere from visible spectroscopy, Planetary and Space Science. 55, 12, 1741-1756, doi:10.1016/j.pss.2007.01.005, 2007.

Wilson, E. L., McLinden, M. L., Miller, J. H., Allan, G. R., Ott, L. E., Melroy, H. R. and Clarke, G. B.: Miniaturized laser heterodyne radiometer for measurements of CO_2 in the atmospheric column, Appl. Phys. B, 114, 385–393, doi:10.1007/s00340-013-5531-1, 2014.

365 Woodman, R. F. and Guillien, A.: Radar observations of winds and turbulence in the stratosphere and mesosphere, J. Atmos. Sci., 31, 493–505, doi:10.1175/1520-0469(1974)031<0493:ROOWAT>2.0.CO;2, 1974.

Wang, J., Wang, G., Tan, T., Zhu, G., Sun, C., Cao, Z., Gao, X., and W. Chen.: Mid-infrared laser heterodyne radiometer (LHR) based on a 3.53 µm room-temperature interband cascade laser, Opt. Express, 27, 9610-9619, doi:10.1364/OE.27.009610 2019.

370 Zenevich, S.G., Klimchuk, A.U., Semenov, V.M., Spiridonov, M.V. and Rodin, A.V.: Measurements of the fully resolved contour of the carbon dioxide absorption line in a band at $\lambda = 1.605$ mm in the atmospheric column using high-resolution heterodyne spectroradiometry method, Quant. Electr., 49, 6, 604–611, doi:10.1070/QEL16859, 2019.

375

Table 1: Observations of CO2 absorption line profile.

Date	Time	Zenith angle, degree	S/N	Position in Figure 5
11.07.2017	11:39	35	96	a
11.07.2017	18:12	69	146	b
02.08.2017	9:11	54	154	c
02.08.2017	9:40	50	193	d
02.08.2017	9:59	48	118	e
02.08.2017	10:22	46	101	f
02.08.2017	10:42	44	101	g
02.08.2017	11:03	42	85	h
02.08.2017	11:23	40	74	i
02.08.2017	11:43	39	94	j
02.08.2017	12:04	38	84	k
02.08.2017	12:25	38	176	l
02.08.2017	12:45	38	110	m
31.08.2017	12:43	47	127	n

380
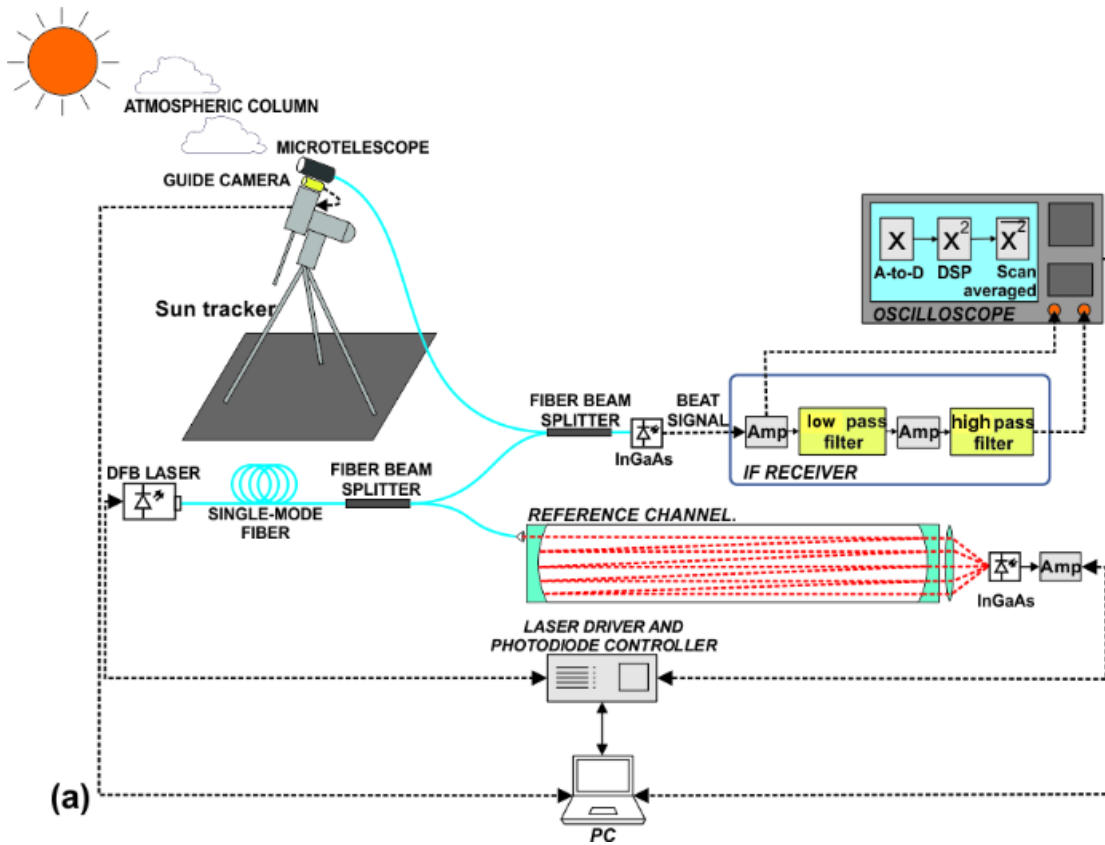
Figure 1: The sketch of laser heterodyne spectrometer used for wind profiling.

a b c
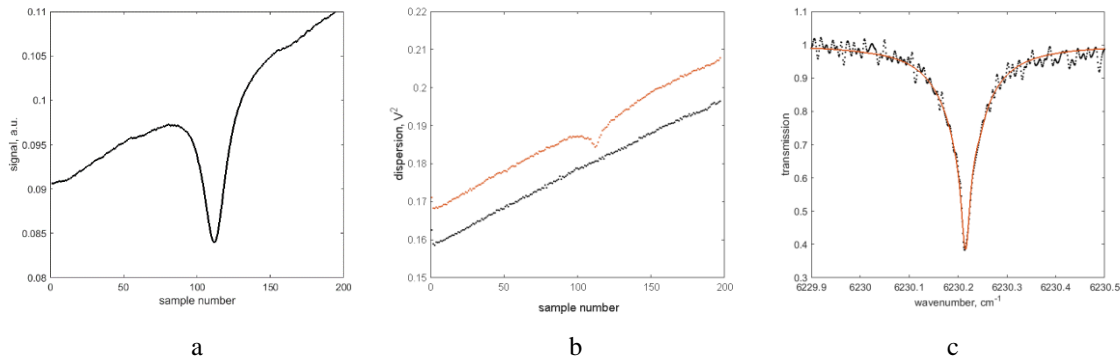
Figure 2: Heterodyne signal treatment in the LHS: (a) signal in the reference channel during one cycle of laser pumping current ramping; (b) noise dispersion in the heterodyne channel during one cycle of laser pumping current ramping; blue dots – with the Sun off, red dots – with the Sun on; (c) atmospheric transmission spectrum obtained after removing dark signal, normalization to suggested continuum (baseline), and frequency calibration. Black dots – experiment, red curve – model fit.
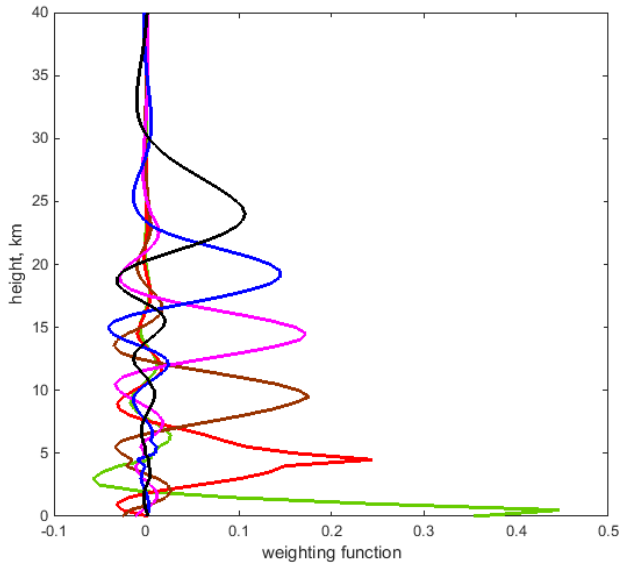
Figure 4: Weighting kernels of wind retrievals according to Eq. (10) as functions of altitude. Kernels corresponding to reference heights of 0, 5, 10, 15, 20, and 25 km are presented.
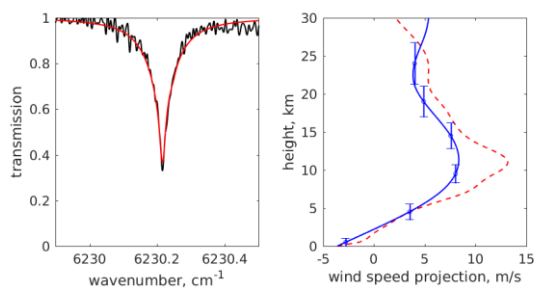
395

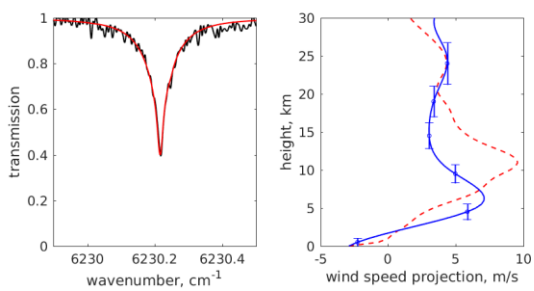
a

b

c

d

e

f

g

h

i

j

k
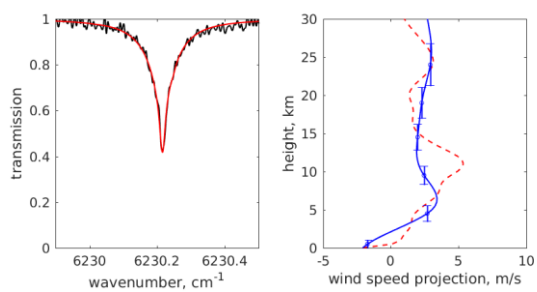
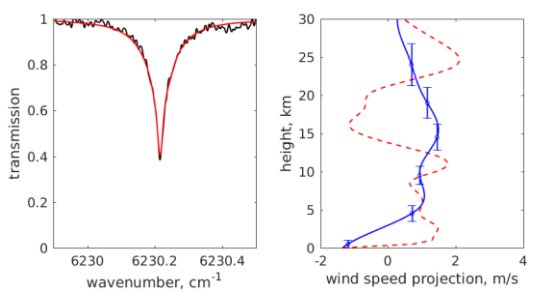l
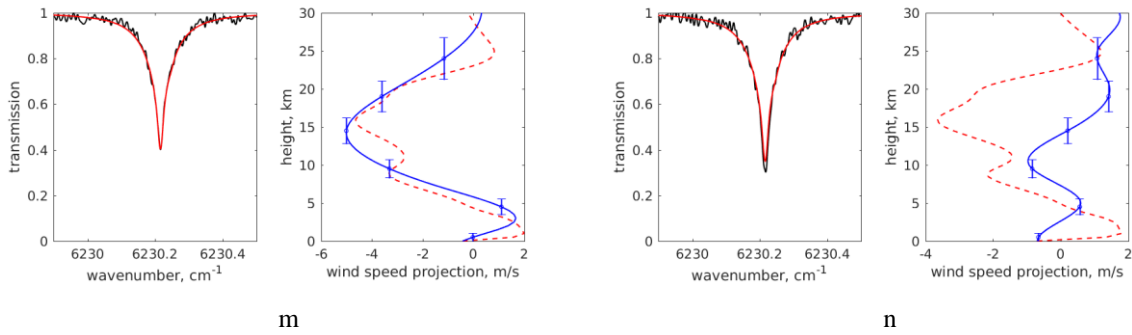
m   n
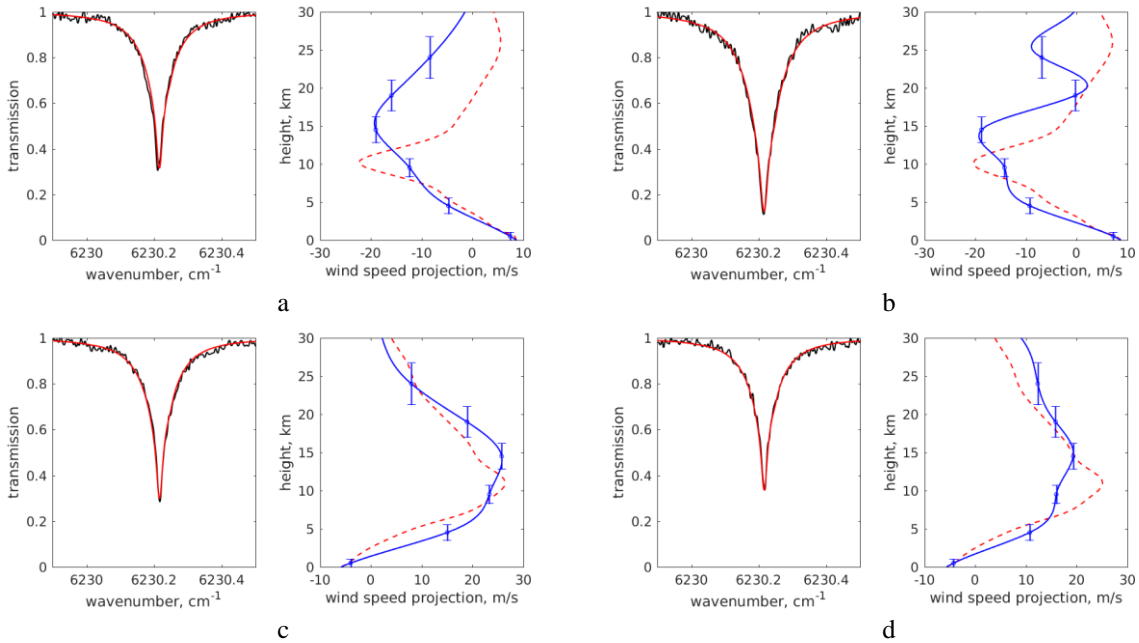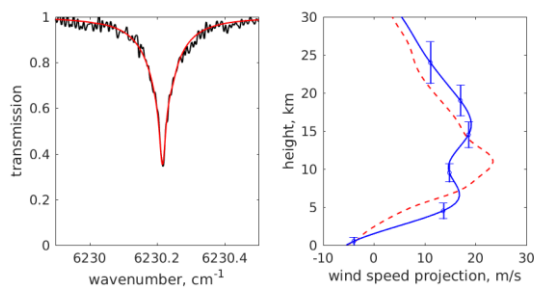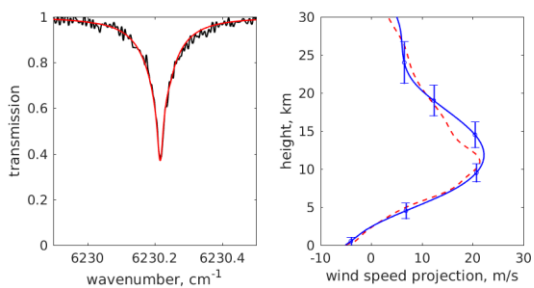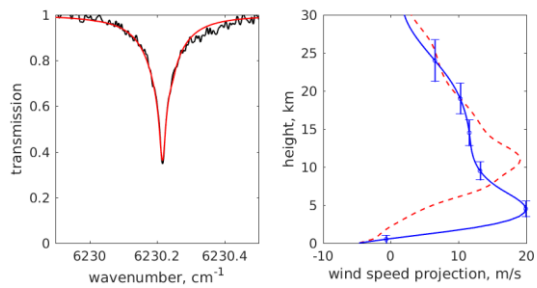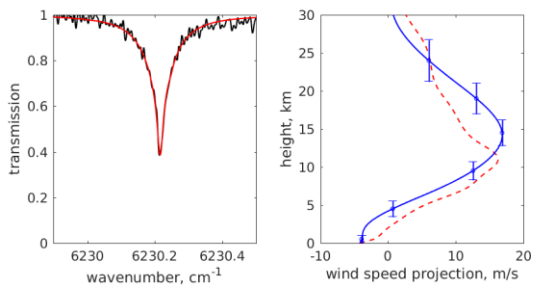
Figure 5: Comparison of retrieved wind projection on the line of sight (right panel, blue curve) with reanalysis data (red dashed curve). Vertical error bars correspond to FWHM of a retrieval averaging kernel presented in Figure 4. Left panel shows atmospheric transmission spectrum measured by means of heterodyne technique (black curve) and corresponding best-fit model spectrum (red curve). Date and local time of each observation are presented in Table 1.